

**This item is the archived peer-reviewed author-version of:**

Applicability of fine industrial metallic iron-rich waste powders for hydrothermal production of hydrogen gas : the influence of non-ferrous contaminants

**Reference:**

Michiels Koen, Haesen Alexander, Meynen Vera, Spooren Jeroen.- Applicability of fine industrial metallic iron-rich waste powders for hydrothermal production of hydrogen gas : the influence of non-ferrous contaminants  
Journal of cleaner production / Masson - ISSN 0959-6526 - 195(2018), p. 674-686  
Full text (Publisher's DOI): <https://doi.org/10.1016/J.JCLEPRO.2018.05.251>  
To cite this reference: <https://hdl.handle.net/10067/1530680151162165141>

# Applicability of Fine Industrial Metallic Iron-Rich Waste Powders for Hydrothermal Production of Hydrogen Gas: the Influence of Non-Ferrous Contaminants

---

Koen Michiels<sup>a,b</sup>, Alexander Haesen<sup>a,†</sup>, Vera Meynen<sup>b</sup> and Jeroen Spooren<sup>a,\*</sup>

<sup>a</sup> Waste Recycling Technologies, Sustainable Materials Management, Flemish Institute for Technological Research, VITO N.V., Boeretang 200, 2400 Mol, Belgium.

<sup>b</sup> Laboratory of Adsorption and Catalysis, Department of Chemistry, University of Antwerp, UAntwerp, Universiteitsplein 1, 2610 Wilrijk, Belgium.

\* Corresponding author. E-mail: [jeroen.spooren@vito.be](mailto:jeroen.spooren@vito.be); phone: +32 14 33 56 33

† Present address: ArcelorMittal Construction Belgium, Geel West Industriezone 4, Lammerdries 8, 2440 Geel, Belgium

Low to negative cost fine industrial metallic iron-rich waste powders are available in large amounts all over the world and are currently often landfilled. The goal of this paper is to investigate the applicability of such waste powders as raw materials for a recently developed hydrothermal hydrogen gas production method, optimised for pure metallic iron powder and operating at a mild hydrothermal temperature of 160 °C for 16 h. The influence of several metallic, oxide and salt compounds of elements ( $M$ ) that are commonly present in metallic iron-rich powder wastes was systematically investigated for two concentration levels,  $(M:Fe)_{low}$  and  $(M:Fe)_{high}$ . The kinetics of hydrogen gas formation was measured during reaction and the obtained solid residues were analysed. This work shows that the oxidation of metallic iron particles and the consequent  $H_2$  gas production in the investigated hydrothermal reaction system were inhibited through three main effects by the here studied contaminants, namely passivation of the reaction surface, carbonate precipitation and/or redox effects. On the other side, Ni addition promotes the reaction kinetics and acts as a catalyst. However, an excess of Ni inhibits complete iron oxidation through fast precipitation of  $Fe_3O_4$  on the metallic iron particle surface, forming a passivation layer.

Finally, three industrial iron waste powders were treated according to the same hydrothermal treatment. Hydrogen gas formation for an iron-rich foundry sand (IWP-A) was inhibited by the formation of a silicate deposit on the iron particles, while the hydrogen gas production from iron works' waste powders (IWP-B and IWP-C) increased with decreasing particle size of the metallic iron particles in the powder.

## 1 Introduction

Recently, Michiels *et al.* [1] demonstrated the production of pressurised hydrogen gas H<sub>2</sub> (purity >99 mol%, P<sub>T=303K</sub> = 15 bar) with a high yield (approximately 80%) *via* a hydrothermal method catalysed by carbonate ions CO<sub>3</sub><sup>2-</sup> and operating at a mild temperature of 160 °C. The hydrogen gas production takes place by reducing water through the oxidation of fine metallic iron powder Fe to iron oxide Fe<sub>3</sub>O<sub>4</sub>, magnetite, according to equation R. 1.



Michiels *et al.* [1] showed that carbonate ions play a key role in the hydrothermal method by enhancing the oxidation of Fe to Fe<sub>3</sub>O<sub>4</sub>. Therefore, hydrothermal Fe oxidation to Fe<sub>3</sub>O<sub>4</sub> is assumed to take place *via* carbonate containing Fe(II) intermediates. On the other hand, Liu *et al.* have catalysed the hydrothermal hydrogen gas production from iron powder through the addition of HCl and Pd [2]. Whereas the individual addition of Pd did not lead to improved H<sub>2</sub> production and Fe oxidation, the combined addition of HCl and Pd did. Pd is believed to enhance the water decomposition through adsorption and activation of water on the Pd surface, while HCl acid accelerates the Fe corrosion by removing the formed iron oxide layer from the surface of iron particles.

Furthermore, small particle sizes for the metallic iron powders are recommended with a preferential particle size of 5 µm or smaller [1, 2]. Though, commercially produced pure fine metallic iron powder is costly due to its (energy) intensive production methods [3].

Alternatively, (fine) metallic iron-rich industrial waste powders are globally available at a much lower cost (magnitude of € 50 per tonne [4]). Such waste powders are produced in iron and steel making and working industries [5]. Since its current reuse and recycling are technically challenging or not economically viable, the waste powders are often being landfilled at a cost [5]. Recently, Crouzet *et al.* [6] produced hydrogen gas by hydrothermal treatment at 300 °C of steel slag, containing partially oxidised iron (FeO) that oxidised to magnetite (Fe<sub>3</sub>O<sub>4</sub>) (R.2).



Furthermore, it was shown that the hydrothermal oxidation of iron can be inhibited, and thus the H<sub>2</sub> production hindered, by the interference of compounds present in the waste. Mg and carbonate ions, which were present in the reaction mixture, precipitated with bivalent iron as (Fe,Mg)-carbonate and so inhibited the further oxidation of iron [6].

The goal of this paper is to investigate the applicability of fine industrial metallic iron-rich waste powders as raw materials for the hydrothermal hydrogen gas production method. The physicochemical quality of a fine metallic iron-rich waste powder varies according to the production process, the used starting materials, the post-processing and its way of storage or disposal [7]. Thus, besides metallic iron, such waste powders often contain oxidised ferrous compounds and other, non-ferrous compounds. Therefore, when applying such powders as feedstock for hydrothermal H<sub>2</sub> production the influence of the present contaminants on the H<sub>2</sub> production process needs to be understood. In this work, three such waste powders are thoroughly characterised and the influence of a broad range of carefully selected individual compounds on the hydrothermal iron oxidation process is investigated.

## **2 Materials and methods**

### **2.1 Materials**

Three industrial waste powders containing metallic iron were studied and are conventionally named IWP-A, IWP-B and IWP-C. IWP-A is the iron-rich fraction of a foundry sand, while IWP-B and IWP-C are obtained from two industries that perform iron and steel works. Based on the characteristics of these waste materials, 20 different analytical grade compounds were selected to investigate their individual influence on the hydrothermal hydrogen gas production reaction method. A list of the compounds used in this work is given further on in the text. The other chemicals used are carbon dioxide CO<sub>2</sub> gas (*Air Products*, >99.5 vol%) and an aqueous potassium hydroxide KOH (*Alfa Aesar*, 85 wt% minimum) solution of 1 M, which was prepared with degassed *Milli-Q* water .

### **2.2 Experimental**

The hydrothermal reactions were performed in stainless steel, stirred 100 mL *Premex reactor ag* autoclaves. A digital control unit and a logging unit allowed for the temperature, pressure and stirring speed to be adjusted and logged online. Inherent to the applied heating system, a short-time temperature overshoot of maximum 5 °C

was observed. However, the temperature set point of 160 °C was reached in less than 30 min from the start of the experiment.

In order to study the influence of individual compounds on the hydrothermal reaction system, 2.24 g (40 mmol) of pure metallic iron powder and an amount corresponding to 0.025 g or 0.25 g of the metal or metalloid element added as a single contaminant (*e.g.* Ca for Ca(OH)<sub>2</sub>) were mixed and loaded in an autoclave. These two elemental weight ratios  $M:Fe = 0.011:1$  and  $0.11:1$  (with  $M$  the elemental metal in the added contaminant) were chosen based on the chemical elemental composition of the industrial waste powders and will be denominated in this work as  $(M:Fe)_{low}$  and  $(M:Fe)_{high}$ , respectively. Next, 40 mL of a 1 M KOH solution was added. Subsequently, the autoclave was flushed with CO<sub>2</sub> gas to remove the contained air and thus create an oxygen free atmosphere. Thereafter, the remaining free space of the autoclave (approximately 60 mL) was filled with 20 mmol CO<sub>2</sub> gas (7 bar at room temperature). The added CO<sub>2</sub> gas quickly dissolved in the liquid phase as carbonate ions, due to the settled equilibria. Finally, the temperature was increased to 160 °C and stirring at 250 rpm was enabled. Reactions were carried out for 16 h, which includes the heating time ( $\pm 30$  min) and excludes the time to cool down to approximately 30 °C. The cooling time was approximately 8 h. Note that some of the experiments are performed under different conditions. In such cases, the reaction conditions are explicitly mentioned.

The same experimental procedure as described above was applied to study fine industrial metallic iron-rich waste powders, wherein 2.24 g of IWP-A, IWP-B or IWP-C were hydrothermally treated.

### 2.3 Analyses

After hydrothermal reaction (*i.e.* when the reactor was cooled down to 30 °C), the gas phase constituents were identified and quantified by coupling the reactor to a *Bruker 450-GC* apparatus (He as carrier gas). The Thermal Conductivity Detector TCD analysed for H<sub>2</sub>, CO<sub>2</sub>, N<sub>2</sub>, CH<sub>4</sub> and CO, while the Flame Ionization Detector FID was used to check for volatile hydrocarbons, other than CH<sub>4</sub>. The applied gas phase analysis allowed to calculate the hydrogen gas yield, *i.e.* the percentage hydrogen yields were calculated based on R. 1 and the ideal gas law, with the measured end pressure at 30 °C, the measured molar percentage of hydrogen gas and the estimated

gas volume as parameters [1]. The hydrogen yields are based on the available amount of iron species which can oxidise with water to form Fe<sub>3</sub>O<sub>4</sub> and H<sub>2</sub> (i.e. metallic Fe, FeO and FeS<sub>2</sub>). The yield is expressed in percentage (%) of mol H<sub>2</sub> produced with respect to the maximal amount of mol of H<sub>2</sub> to be able to be produced (i.e. if all Fe would be oxidised to Fe<sub>3</sub>O<sub>4</sub>) with the content of oxidisable Fe species present in the specific mixture.

Subsequently, the solid phase and liquid phase were rapidly separated over a *Whatman mixed cellulose ester membrane filter ME25* (0.45 µm pore size). The solid phase was dried and stored under an oxygen free atmosphere.

The amount of non-purgeable organic carbon NPOC present in the liquid phases was determined (*Analytik Jena AG multi N/C 3100*) to obtain insight in the converted amount of hydrogen gas by CO<sub>2</sub> hydrogenation. Furthermore, liquid samples were analysed by Inductively Coupled Plasma Atomic Emission Spectroscopy ICP-AES (*THERMO OPTEK IRIS ADVANTAGE*) in order to measure the concentration of dissolved elements. Therefore, the liquid samples were prepared by conserving the liquid phase by addition of 2 vol% HNO<sub>3</sub> 67-69 wt% of *OPTIMA Acids Fisher Scientific* and diluting with *Milli-Q* water.

The solid starting materials and residues after reaction were characterised by several methods. The elemental composition of starting materials was determined by Energy Dispersive X-Ray Fluorescence EDXRF analyses (*Thermo Fisher Scientific Niton XL3 Analyzer*) and the mineralogy of the solid samples by X-ray powder diffraction XRD (*PANalytical X'PERT PRO* (Cu-anode), *ICDD* [8] database). Rietveld quantitative analyses (*ICSD* [9]) of the obtained diffractograms of commercial starting materials allowed for semi-quantification of the mineral phases. Quantitative XRD analyses of the waste materials were performed by another system (*PANalytical EMPYREAN* (Co anode)) applying an external standard (TiO<sub>2</sub>, *Kronos International*). Scanning Electron Microscopy SEM images (*JEOL JSM-6340F* and/or *FEI Nova NanoSEM 450*) of the residue powders allowed for determination of morphology and elemental mapping (*Bruker XFlash Detector 5030* or *Bruker QUANTAX 200* EDS system). Prior to SEM measurements, the waste powders were embedded in an epoxy resin and subsequently polished. Furthermore, particle size distribution measurements of starting materials were performed by laser diffraction (*Microtrac S3500*).

### 3 Results and discussion

#### 3.1 Properties of fine industrial waste powders containing metallic iron

The elemental compositions of the fine industrial metallic iron containing waste powders IWP-A, IWP-B and IWP-C are shown in Table 1. The concentration of elemental Fe in IWP-A is 40 wt%, whereas IWP-B and IWP-C contain approximately 80 wt% elemental Fe. The elements Ca, K, Ni, S and Zr are only present in IWP-A. Moreover, the concentrations of elemental Al, Cr and Si in IWP-A are significantly higher in comparison with the other two industrial waste powders, whereas the Mn concentration is comparable for all three powders.

Table 1. Elemental composition of IWP-A, IWP-B and IWP-C, obtained *via* EDXRF analyses. The significant concentrations (*i.e.* >0.50 wt%) are given in bold

Element	IWP-A (wt%)	IWP-B (wt%)	IWP-C (wt%)
Al	<b>4.4</b>	<b>1.7</b>	0.33
As	0.01	<LOD	<LOD
Ba	0.02	<LOD	0.03
Ca	<b>1.0</b>	0.06	0.22
Cl	0.09	<LOD	0.04
Cr	<b>3.2</b>	0.38	<b>0.58</b>
Cu	0.05	0.02	0.05
Fe	<b>40</b>	<b>82</b>	<b>80</b>
K	<b>1.1</b>	0.09	0.08
Mg	<LOD	<b>4.0</b>	<LOD
Mn	<b>0.60</b>	<b>0.60</b>	<b>0.74</b>
Mo	0.18	0.01	0.01
Nb	0.01	<LOD	<LOD
Ni	<b>0.96</b>	<LOD	0.03
Pb	0.01	0.03	0.03
S	<b>2.2</b>	0.04	0.11
Si	<b>10</b>	<b>0.73</b>	<b>0.87</b>
Sn	0.01	0.01	0.01
Sr	0.01	<LOD	<LOD
Ti	0.31	<LOD	0.02
V	0.06	0.02	0.03
Zn	0.02	<LOD	0.02
Zr	<b>2.3</b>	0.01	<LOD

LOD: Limit of Detection

As light elements such as O, C, H and N cannot be detected by the elemental analysis and several elements can form a wide variety of crystal structures, XRD analysis has been performed. The iron containing crystalline phases hematite  $\text{Fe}_2\text{O}_3$ , magnetite  $\text{Fe}_3\text{O}_4$ , wüstite  $\text{FeO}$  and metallic iron  $\text{Fe}$  are present in all three waste powders (Figure 1). Exclusively IWP-A contains pyrite  $\text{FeS}_2$ . In contrast to IWP-C, IWP-A and IWP-B contain non-ferrous crystalline phases, such as corundum  $\alpha\text{-Al}_2\text{O}_3$ . Additionally, in IWP-A calcite  $\text{CaCO}_3$ , moissanite  $\text{SiC}$ , quartz  $\text{SiO}_2$ , zirconium silicate  $\text{ZrSiO}_4$  and spinel phases were found. Quantitative XRD analyses allowed determining the available amounts of zero-valent (metallic  $\text{Fe}$ ) and bi-valent ( $\text{FeO}$  and  $\text{FeS}_2$ ) iron within the samples. IWP-A, IWP-B and IWP-C contain 21 wt%, 80 wt% and 49 wt% of metallic  $\text{Fe}$ , respectively and 9 wt%, 7 wt% and 20 wt% of  $\text{FeO}$ , respectively. Furthermore, IWP-A contains 2 wt% of pyrite. Assuming that these minerals can potentially oxidise to  $\text{Fe}_3\text{O}_4$ , the theoretical  $\text{H}_2$  production potentials for IWP-A, IWP-B and IWP-C are 5.5 mmol/g, 19 mmol/g and 13 mmol/g, respectively.

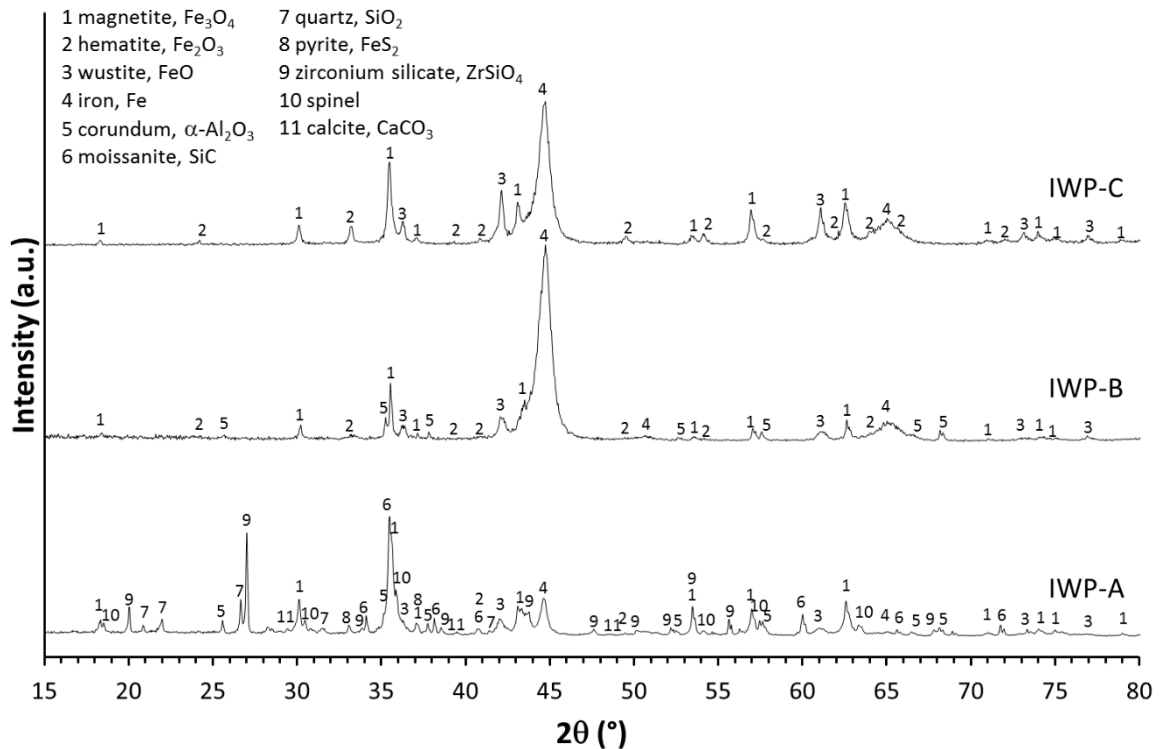


Figure 1. X-ray powder diffractogram of the fine industrial metallic iron-rich waste powders. The identified crystalline phases are assigned.

All three industrial waste powders have a broad particle size distribution in the micrometre range (Supplementary Data). IWP-A contains the finest particles ( $d_{50} = 15.4 \mu\text{m}$ ), followed by IWP-C ( $d_{50} = 31.6 \mu\text{m}$ ) and IWP-B ( $d_{50} = 42.6 \mu\text{m}$ ).

Figure 2 shows SEM-BSE (Back-Scattered Electrons) and SEM-EDS images of the studied industrial waste powders. These images confirm that IWP-A contains the least elemental Fe, of which a substantial fraction is (partially) oxidised. In IWP-A, metallic iron is present in small separated particles (up to  $10 \mu\text{m}$ ), as well as in larger aggregated particles ( $> 20 \mu\text{m}$ ). Further, IWP-B and IWP-C contain significant quantities of ‘rounded’ and/or ‘needle-shaped’ ( $< 100 \mu\text{m}$ ) individual metallic iron particles.

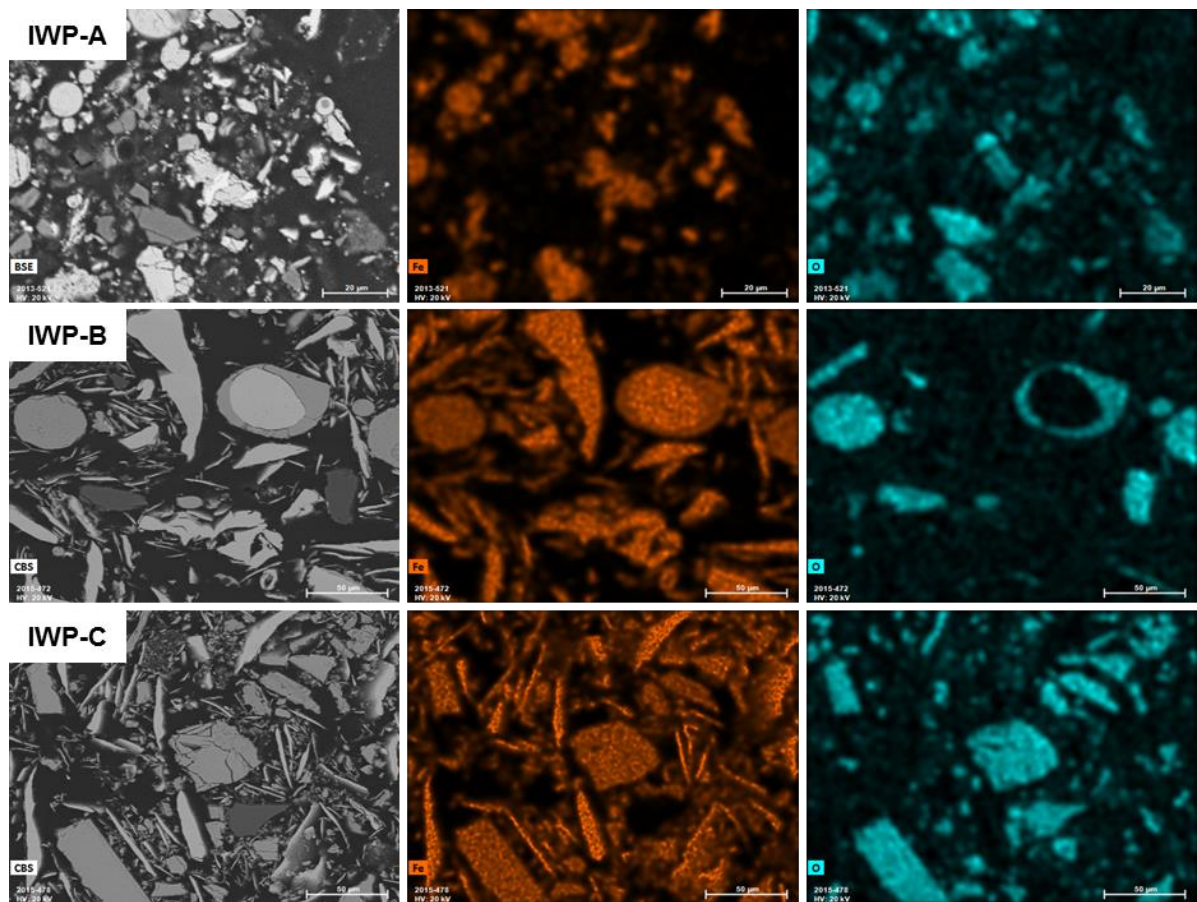


Figure 2. SEM-BSE images and corresponding elemental maps (SEM EDS) of Fe and O of the studied fine grained iron-rich industrial waste powders.

In order to understand the behaviour of metallic iron-rich industrial waste powders in the hydrothermal hydrogen gas production system, the behaviour of the individual compounds/contaminants, present in these iron waste powders, needs to be understood first. Therefore, based on the characteristics of the studied industrial metallic iron-rich waste

powders and general compositions of steel alloys [10], 20 commercially available compounds were selected. These materials include zero-valent metal powders, metal oxides and metals salts. Although elemental contaminants in waste materials are mostly present in more complex forms (e.g. alloys, spinels, silicates, solid solutions, etc.), we believe to have selected a representative set of model compounds. Table 2 shows the selected compounds and their suppliers. The crystalline compositions and particle size distributions of these powders were analysed (see Supplementary Data) in order to determine the exact composition and speciation of elements in these powders.

Table 2. Overview of the used commercial powders and their suppliers (for detailed information see Supplementary Data).

<b>Compound</b>	<b>Supplier</b>	<b>Compound</b>	<b>Supplier</b>
Fe	<i>Merck Millipore</i>	TiO <sub>2</sub>	<i>Du Pont</i>
Mn	<i>Goodfellow Cambridge Ltd.</i>	V <sub>2</sub> O <sub>5</sub>	<i>Fisher Scientific Company</i>
Zn	<i>Umicore</i>	MnO	<i>BassTech International</i>
Cr	<i>CERAC</i>	SiO <sub>2</sub>	<i>Sibelco Benelux</i>
Ni	<i>Aldrich Chemical Company, Inc.</i>	ZnO	<i>UCB</i>
Mo	<i>Dr. Theodor Schuchardt</i>	Cr <sub>2</sub> O <sub>3</sub>	<i>Riedel-de Haën</i>
Cu	<i>Johnson Matthey</i>	Co <sub>3</sub> O <sub>4</sub>	<i>Janssen Chimica</i>
Ca(OH) <sub>2</sub>	<i>AnalaR NORMAPUR</i>	NiO	<i>CERAC</i>
CaCO <sub>3</sub>	<i>J.T. Baker Chemicals B.V.</i>	MoO <sub>3</sub>	<i>Merck</i>
MgO	<i>Johnson Matthey</i>	CuO	<i>Riedel-de Haën</i>
( $\alpha$ -)Al <sub>2</sub> O <sub>3</sub>	<i>Almatis</i>		

## **3.2 Influence of individual compounds on the hydrothermal hydrogen gas production via the oxidation of metallic iron**

### **3.2.1 Reference experiment with pure metallic iron powder**

A hydrothermal benchmark experiment was performed with pure metallic iron powder of an average particle size of 10  $\mu$ m (Table 2). After reaction, gas phase analyses showed the presence of hydrogen gas (>99 mol%) and a small amount of carbon dioxide gas (<1 mol%). The derived hydrogen gas yield amounted to approximately 76%. This result is in line with previously reported yields for the same type of reaction with pure metallic iron powder with an average particle size of 5  $\mu$ m [1].

At a fill ratio of 40% the partial water pressure in the autoclave system at 160 °C equals the water vapour pressure of 6.18 bar at that temperature [11]. In the studied

system, the partial pressure of water remains approximately constant at a constant temperature. Thus, the reactor pressure evolution during reaction at constant temperature of 160 °C gives a direct measurement of the amount of produced hydrogen gas in time and thus provides information on the reaction kinetics. Figure 3 (top) shows a typical pressure evolution curve, measured during the reference experiment. Together with the pressure evolution curve, the online measurement of the temperature inside the reactor vessel is plotted and shows that initially the temperature rises to the set reaction temperature of 160 °C. From the pressure evolution curve we derived the effective reaction time  $t_e$ , as the time span after which the reactor pressure becomes constant and thus the hydrogen gas formation stopped. A difference of  $\geq 2$  h between two  $t_e$  values is defined as significant. Furthermore, the hydrogen formation reaction kinetics can be derived from the measured pressure evolution curves *via* two approaches. Both methods fit a function to the experimentally obtained pressure curves when the reaction temperature is constant at 160 °C. In a first method, reaction rates were calculated in  $\text{bar h}^{-1}$ , based on fitting the initial part of the pressure increase over time by a zero order reaction linear function  $P = P_0 + kt$ , where  $P$  is the pressure at time  $t$ ,  $P_0$  is a constant and  $k$  is the reaction rate constant in  $\text{bar h}^{-1}$  (Figure 3, bottom left). For the reference experiment, a straight line with a slope of  $2.8 \text{ bar h}^{-1}$  is following the initial rise in reactor pressure from 0.6 h up to 2.5 h. Hence,  $k = 2.8 \text{ bar h}^{-1} [0.6 \text{ h}; 2.5 \text{ h}]$ . The zero order reaction kinetics only occurs at the start of the reaction when reagents are abundant and the reaction is not yet governed by diffusion effects that generally occur in a shrinking core reaction model [12]. The latter is believed to take place in the studied systems [1, 13], whereby reaction of the metallic iron particles proceeds from the outer layers of the particle towards its core. The second method to derive kinetic information from the pressure curves takes into account the progressive diminution of the reaction rate by fitting a Boltzmann derived function  $P = P'_{max} + ((P'_0 - P'_{max}) / (1 + \exp(k't)))$  to the pressure evolution curve during the period that the reaction temperature is constant at 160 °C (Figure 3, bottom right). In this function,  $P'_{max}$  is the final maximal pressure of produced  $\text{H}_2$  that can be attained in the reactor at 160 °C for the studied reaction,  $P'_0$  is a constant and  $k'$  is the reaction rate constant in  $\text{h}^{-1}$ . In the case of fitting the Boltzmann equation, the time, reported on the horizontal axis, is set to  $t = 0$  when the reaction temperature of 160 °C is reached.

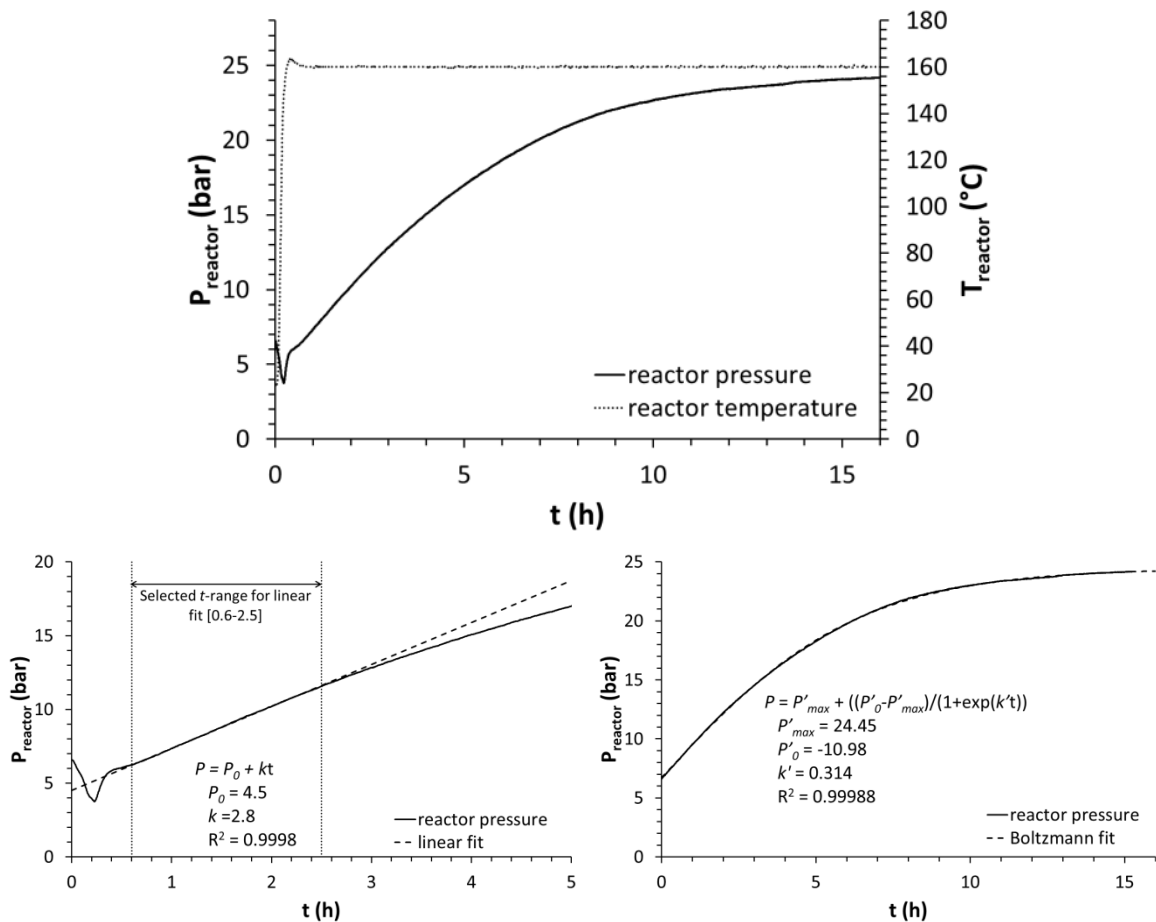


Figure 3. Top: Evolution in reactor pressure and temperature over time for the reference experiment. Bottom left: Linear curve fit (zero order equation) of the reactor pressure at start of the reaction. Bottom right: Derived Boltzmann equation curve fit of the reactor pressure.

### 3.2.2 Influence of individual contaminants on the hydrothermal H<sub>2</sub> gas production from metallic iron powder

Individual compounds were added to the studied hydrothermal reaction system at two different weight ratios with respect to a fixed amount of iron present in the reaction system. The pressure evolutions logged during the reactions are shown in Figure 4 for each individual compound and are compared to the pressure evolution curve of the reference experiment. As can be observed, reaction kinetics and reaction yields differ depending on the added contaminant and its concentration.

Similarly to the reference experiment, we assume that no hydrogen was consumed through reaction with CO<sub>2</sub> and/or carbonates, since no CO, CH<sub>4</sub> or other hydrocarbons were detected in the gas phase and the measured NPOC concentration in the liquid phase was negligible.

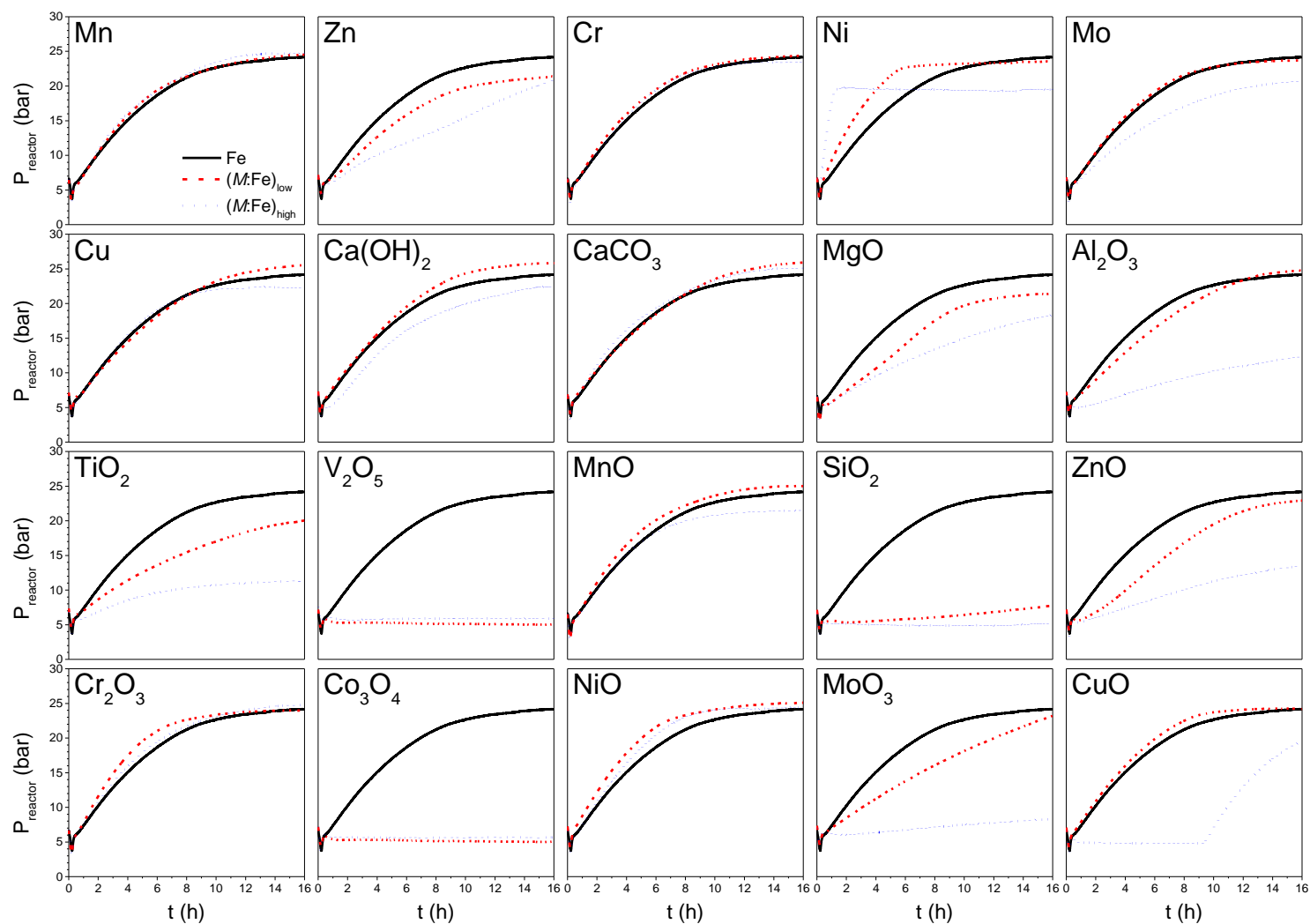


Figure 4. Pressure evolution curves of the hydrothermal hydrogen production reactions whereby Fe is reacted in a 1 M KOH solution in the presence of dissolved CO<sub>2</sub> gas at a temperature of 160°C and an added individual contaminant at two different addition ratios.

Figure 5 shows the rate constant  $k'$  obtained through fitting of the experimental pressure curves for the experiments with  $(M:Fe)_{low}$  and  $(M:Fe)_{high}$  contaminant addition, respectively, as well as the experimentally observed  $H_2$  yield at the end of each experiment. A complete overview of the kinetic fitting parameters and experimental numeric data is given in the Supplementary Data.

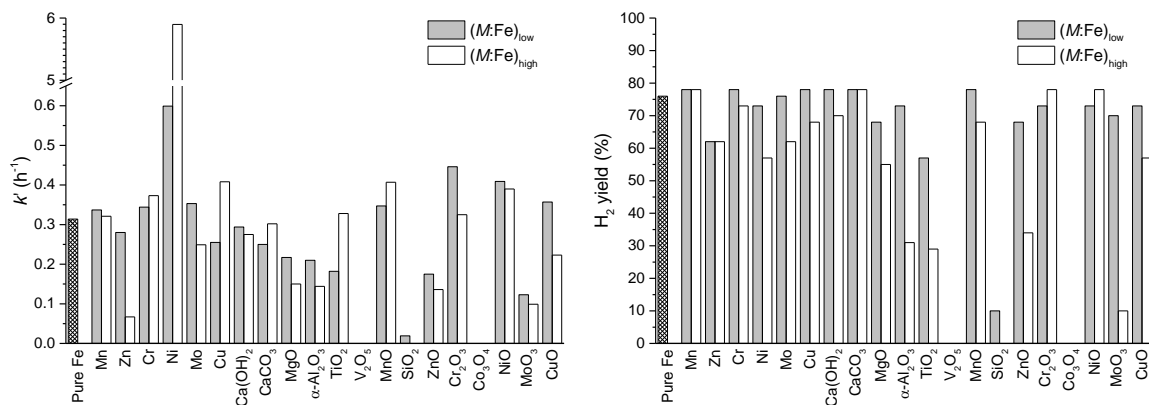


Figure 5. Fitted rate constant  $k'$  (left) and measured  $H_2$  yield (right) for the experiments with  $(M:Fe)_{low}$  and  $(M:Fe)_{high}$  contaminant addition and the reference experiment with pure iron.

Analyses of the reaction pressure curves (Figures 4-5 and Supplementary Data) show that several tested compounds influence the reaction kinetics of hydrogen gas formation in the studied hydrothermal system. It is the aim of this work to understand the effects that can occur for each individual compound on the studied reaction system. These effects are described in detail below and can be categorised as follows:

- (i) Promoting kinetic effects;
- (ii) Inhibition through fixating carbonate ions that catalyse the iron oxidation reaction;
- (iii) Inhibition through forming a passivation layer on the metallic iron particles;
- (iv) Inhibition through redox effects.

### 3.2.2.1 Promoting kinetic effects

The presence of Ni in the reaction slurry in a 0.01 Ni:Fe ratio led to a noticeable increase of the reaction rate constant  $k'$  of 90% and reduction of the reaction duration ( $t_e$ ). Figure 6 shows the pressure evolutions for different tested Ni:Fe ratios (*i.e.* 0.2,

0.1, 0.05, 0.03, 0.02 and 0.01), the fitted reaction rate constant  $k'$  and obtained  $H_2$  yields. Clearly,  $k'$  increases as a function of Ni addition and consequently,  $t_e$  decreases. However, concurrently the  $H_2$  yield decreases upon Ni addition and thus less iron was oxidised as observed by XRD (Supplementary Data). In the case of Ni:Fe = 0.2, the reaction halted before the reactor temperature reached the set temperature of 160 °C.

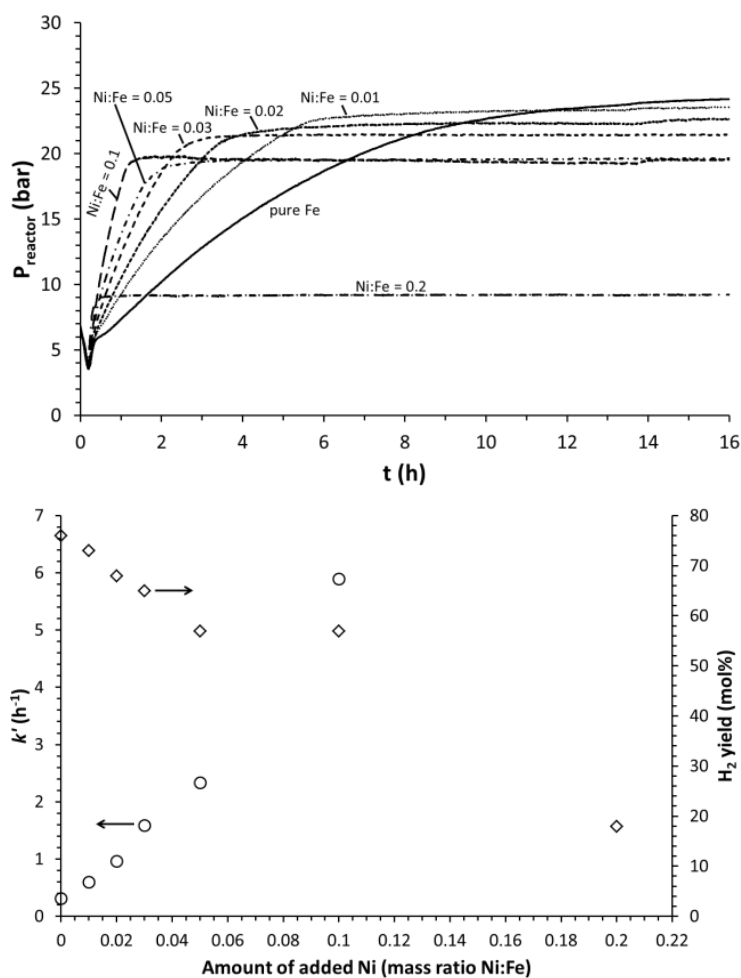


Figure 6. Top: Evolutions in reactor pressure over time for the experiments that apply different amounts of Ni as tested compound. Bottom: fitted  $k'$  reaction rate constant and observed  $H_2$  yield as a function of Ni addition to the reaction mixture.

XRD analyses of the obtained residues did not reveal the presence of oxidised Ni (Supplementary Data) and neither did the reaction liquid contain dissolved Ni, as measured by ICP-AES. Therefore, Ni is not consumed during reaction and improves the reaction kinetics, which indicates catalytic activity. Actually, Ni-based catalysts are applied for the

hydrogen evolution reaction, which is a half reaction of water splitting that reduces protons into hydrogen gas (*i.e.* it reduces water in alkaline medium) [14, 15].

SEM-EDS analyses (Figure 7) show a large amount of aggregated oxidised Fe particles when Ni was added in a 0.01 ratio to Fe. Upon further addition of Ni, oxidised iron can only be observed deposited as an outer layer on metallic iron particles. The thickness of this layer reduced when more Ni was added. It is believed, in the light of the shrinking core reaction model that during reaction Fe dissolves at the metallic particle surface and consecutively precipitates as  $\text{Fe}_3\text{O}_4$ , which is stable. Thus we believe that increasing reaction kinetics inhibit the diffusion of dissolved Fe away from the metallic iron particle by a faster precipitation of iron oxide on the metallic iron particle. Consequentially, metallic iron particles are passivated faster when Ni is present in the studied reaction system.

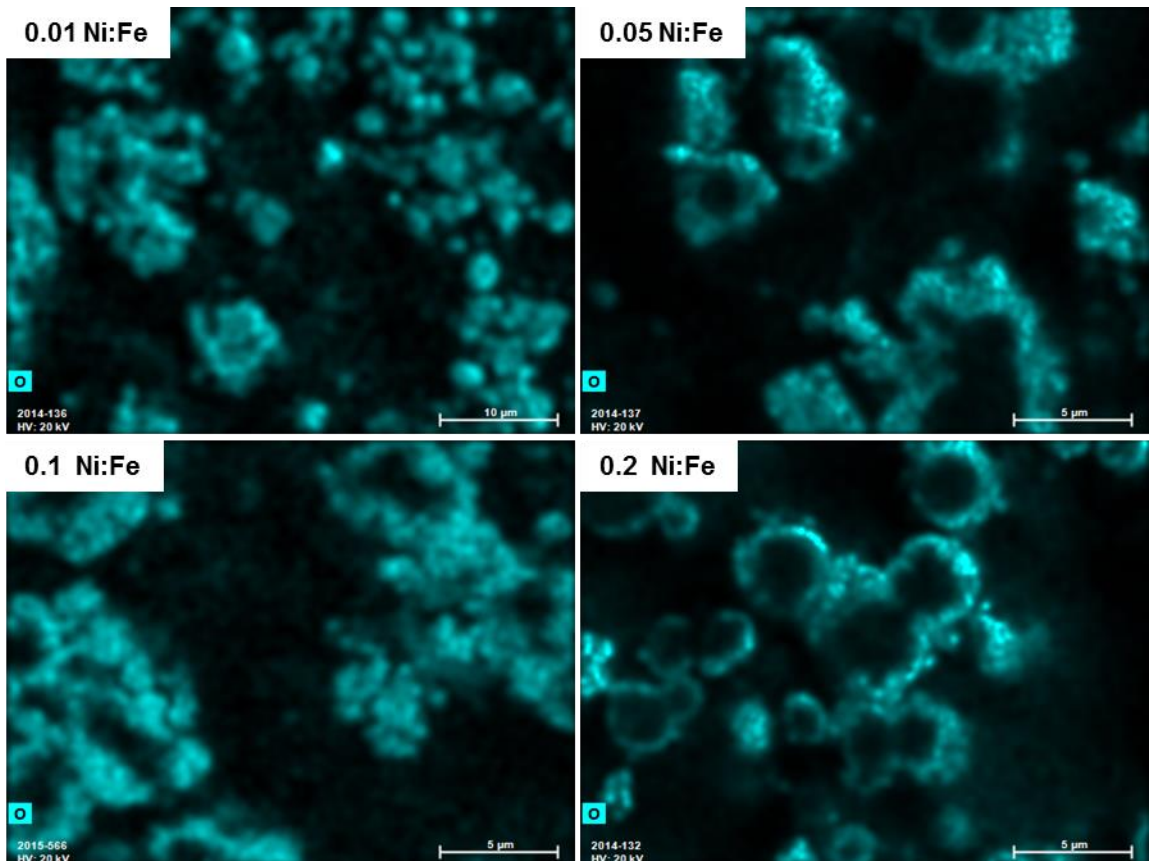


Figure 7. SEM-EDS oxygen mapping of reaction residues. The oxygen is exclusively associated to  $\text{Fe}_3\text{O}_4$ .

Low concentration additions ( $(M:Fe)_{low}$ ) of the transition metal oxides  $Cr_2O_3$ , NiO, CuO and MnO increased the kinetics of the hydrogen gas formation slightly. In the case of  $Cr_2O_3$  and NiO this effect is clearly observed, while for CuO and MnO it is less pronounced (Figure 4).

### 3.2.2.2 Inhibition through carbonate formation

Carbonate phases formed when performing experiments with Mn, MnO,  $Ca(OH)_2$  and MgO (Supplementary Data). Mn addition did not promote nor inhibit hydrogen production with respect to the reference (pure Fe) experiment. For  $Ca(OH)_2$ , MnO and MgO, a higher concentration of added contaminants  $(M:Fe)_{high}$ , led to a stronger inhibition of the hydrogen production (Figure 5). However, the higher amount of formed carbonates at  $(M:Fe)_{high}$  with respect to  $(M:Fe)_{low}$  addition did not decrease the amount of produced  $Fe_3O_4$  and  $H_2$  proportionally. Actually, SEM images (Figure 8) show that most carbonate phases did not precipitate onto the surface of the iron particles. Only in the case of  $Ca(OH)_2$  addition, a thin  $CaCO_3$  layer can be observed near the surface of  $Fe_3O_4$  particles, indicating that  $CaCO_3$  was deposited after precipitation of  $Fe_3O_4$ . Thus, the majority of iron particles were not directly passivated by a carbonate surface layer.

In the case of Mn, the  $H_2$  yield did not decrease (Figure 5). However, XRD and SEM analyses of the solid residues showed that partial oxidation of Mn took place, leading to the formation of manganese(II) carbonate  $MnCO_3$  (rhodochrosite) (Supplementary Data). In the solid obtained through the experiment of  $(M:Fe)_{high}$  Mn, XRD semi-quantification estimated the presence of 7.2 wt%  $MnCO_3$ . In SEM images separate Fe and Mn containing particles were observed, suggesting that clustering did not occur (Figure 8).

When  $CaCO_3$  was directly added to the reaction mixture a slight increase in  $H_2$  gas formation was observed (Figure 4). This indicates that already formed carbonate phases, which are not deposited on the surface of iron particles, do not influence the iron oxidation reaction negatively. Furthermore, a partial dissolution of  $CaCO_3$  allows for a higher amount of dissolved carbonate ions to take part in the carbonate catalysed hydrothermal iron oxidation. Therefore, given the catalytic role of carbonate ions in the hydrothermal hydrogen gas production from metallic iron [1], we assume that the precipitation of carbonate salts capture carbonate ions from the reaction solution with a consequent slowing down of reaction kinetics.

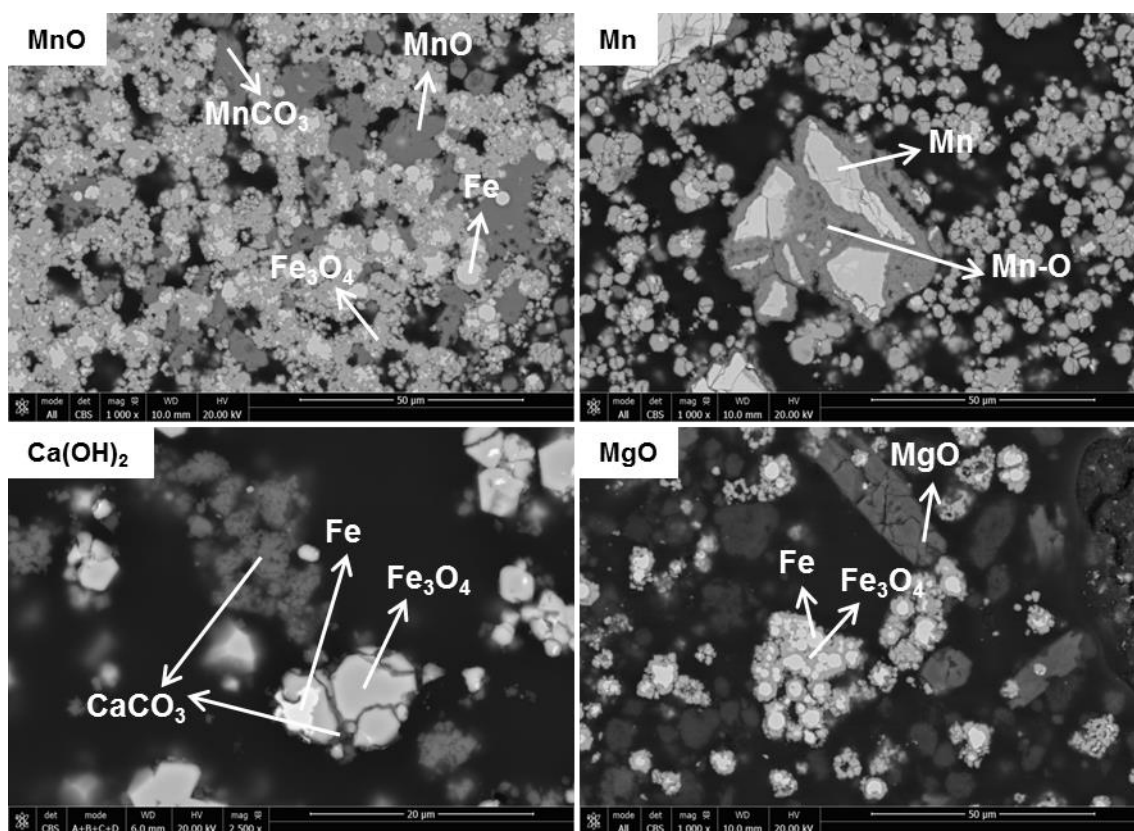


Figure 8. SEM images of the residues after hydrothermal reaction with  $(M:Fe)_{high}$  of possible carbonate forming materials (MnO, Mn,  $Ca(OH)_2$  and MgO).

### 3.2.2.2 Inhibition through formation of a passivation layer on iron particles

Generally, elements in a bi- or tri-valence state could be incorporated into the  $Fe_3O_4$  crystal lattice to form spinel phases. In order to detect whether cations, other than  $Fe^{2+}$  and  $Fe^{3+}$  became incorporated in the cubic crystal lattice ( $Fd3m$ ) of  $Fe_3O_4$  during the hydrothermal formation of this mineral phase, the characteristics magnetite peaks in the XRD diffractogram of the obtained solids were analysed for shifts in peak positions. Rietveld refinement of the magnetite peaks in the XRD diffractogram of the residue produced in the reference experiment (pure Fe) gave  $a = 8.396 \text{ \AA}$ , which is equal to the value for the  $Fd3m$  space group of magnetite ( $Fe_3O_4$ ) as reported in the literature [16]. Table 3 reports the compounds for which the unit cell parameter  $a$  of the measured  $Fe_3O_4$  pattern differed from the reported  $Fe_3O_4$  value. It is shown that  $(M:Fe)_{high}$  of Mo,  $MoO_3$ , MnO, Zn, ZnO and  $Al_2O_3$  did result in a co-precipitation of iron and the contaminant metal as an oxide, whereby bivalent cations of Mo, Mn and

Zn partially substitute  $\text{Fe}^{2+}$  at the *A*-sites in the  $\text{Fe}_3\text{O}_4$  spinel  $\text{AB}_2\text{O}_4$  lattice, while the trivalent  $\text{Al}^{3+}$  partially replaced  $\text{Fe}^{3+}$  ions at the *B*-sites. Iron spinel phases containing Mo, Mn, Zn and Al have been reported as  $\text{MoFe}_2\text{O}_4$  (Fd3m,  $a = 8.41\text{-}8.42 \text{ \AA}$ ) [17],  $\text{MnFe}_2\text{O}_4$  (jacobsonite, Fd3m,  $a = 8.457 \text{ \AA}$ ) [18],  $\text{ZnFe}_2\text{O}_4$  (franklinite, Fd3m,  $a = 8.452 \text{ \AA}$ ) and  $\text{FeAl}_2\text{O}_4$  (hercynite, Fd3m,  $a = 8.119 \text{ \AA}$ ), respectively. Therefore, the unit cell parameter  $a$  of the Mo, Mn and Zn containing iron spinel is larger than that for pure  $\text{Fe}_3\text{O}_4$  and indeed a shift to higher values is observed as a function of the added concentration of compounds containing these metals (Table 3). While for  $\text{Al}_2\text{O}_3$  addition a shift to a lower  $a$  value as function of the added concentration is observed (Table 3). Yi *et al.* reported the hydrothermal synthesis of ferrite spinel particles from dissolved metal ions at temperatures in the range of 130-150 °C and a pH of 7-8 [19], which are similar to the reaction conditions in this work.

Table 3. Derived Fd3m unit cell parameter (Rietveld refinement) of the  $\text{Fe}_3\text{O}_4$  peaks in the XRD diffractogram on the residue obtained after hydrothermal treatment of metallic iron and added contaminants.

<b>Contaminant added</b>	<b>Added concentration</b>	<b>XRD derived Fd3m unit cell parameter <math>a</math> (Å)</b>
Pure Fe	/	8.396
Mo	$(M:\text{Fe})_{\text{low}}$	8.397
Mo	$(M:\text{Fe})_{\text{high}}$	8.399
$\text{MoO}_3$	$(M:\text{Fe})_{\text{low}}$	8.399
$\text{MoO}_3$	$(M:\text{Fe})_{\text{high}}$	8.404
MnO	$(M:\text{Fe})_{\text{low}}$	8.397
MnO	$(M:\text{Fe})_{\text{high}}$	8.404
$\text{Al}_2\text{O}_3$	$(M:\text{Fe})_{\text{low}}$	8.392
$\text{Al}_2\text{O}_3$	$(M:\text{Fe})_{\text{high}}$	8.381
Zn	$(M:\text{Fe})_{\text{low}}$	8.399
Zn	$(M:\text{Fe})_{\text{high}}$	8.416
ZnO	$(M:\text{Fe})_{\text{low}}$	8.399
ZnO	$(M:\text{Fe})_{\text{high}}$	8.426

In the presence of  $(M:Fe)_{low}$   $SiO_2$  a very slow and limited production of  $H_2$  gas was observed (Figure 4), while for  $(M:Fe)_{high}$   $SiO_2$  no  $H_2$  production took place. The iron oxidation reaction with consequential  $H_2$  production was hindered and fully blocked at  $(M:Fe)_{low}$   $SiO_2$  and  $(M:Fe)_{high}$   $SiO_2$ , respectively. SEM images (Figure 9) and elemental mapping clearly show encapsulation of the metallic iron particles by a thin layer of an oxide material rich in K, Fe and some Si. Due to the limited thickness of this layer, XRD analyses (Supplementary Data) could not determine the mineralogy of this phase. Hydrothermal synthesis of silicates has been reported in literature, and in particular silicates such as potassium ferrisilicate  $KFeSiO_4$  and potassium silicate [20].

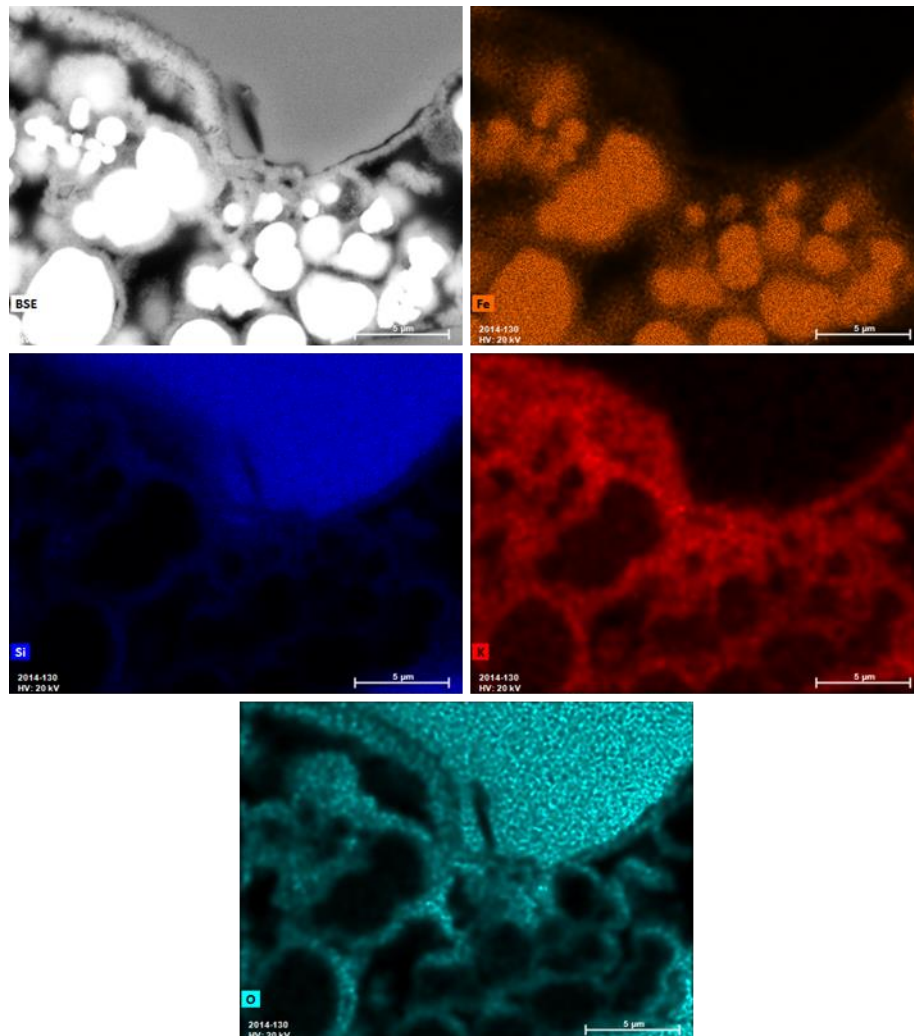


Figure 9. SEM-BSE and SEM-EDS images for Fe, Si, K and O of the solid obtained through the  $(M:Fe)_{high}$   $SiO_2$  experiment.

In several cases, oxidised iron was found in the resulting residue as a carbonate hydroxide  $\text{Fe}_2\text{CO}_3(\text{OH})_2$ , chukanovite (Figure 10). This iron carbonate hydroxide phase occurred in some solid residues when the hydrogen production was strongly, but not fully hindered (see Figure 4) by the added compounds  $\text{MoO}_3$  ( $(M:\text{Fe})_{\text{low}}$ ),  $\text{Zn}$  ( $(M:\text{Fe})_{\text{high}}$ ),  $\text{ZnO}$  ( $(M:\text{Fe})_{\text{high}}$ ),  $\text{SiO}_2$  ( $(M:\text{Fe})_{\text{low}}$ ) and  $\text{Al}_2\text{O}_3$  ( $(M:\text{Fe})_{\text{high}}$ ). Chukanovite is a corrosion product of iron and steel in carbonate-containing environments [21]. Chukanovite is metastable with respect to siderite ( $\text{FeCO}_3$ ) independent of pH and carbonate concentration and can be formed by corrosion of iron in anoxic neutral and alkaline media. Furthermore, Chen *et al.* showed that the ratio of  $\text{Fe}^{2+}$  and  $\text{OH}^-$ , as well as that of  $\text{CO}_3^{2-}$  and  $\text{OH}^-$  determine the formation of chukanovite in solution, which is stable in the potential-pH region of  $-740 \text{ mV} < \text{Eh} < -400 \text{ mV}$  and  $7.87 < \text{pH} < 10.34$  [22]. In the case of  $\text{Al}_2\text{O}_3$  addition an iron aluminium hydroxide carbonate was formed. Chukanovite and aluminium hydroxide carbonate do not cause the inhibition of iron oxidation but are rather formed as a consequence of incomplete iron oxidation to magnetite ( $\text{Fe}(+\text{II})\text{Fe}(+\text{III})_2\text{O}_4$ ). Namely, these minerals precipitate excess bivalent Fe ( $\text{Fe}^{2+}$ ) from solution.

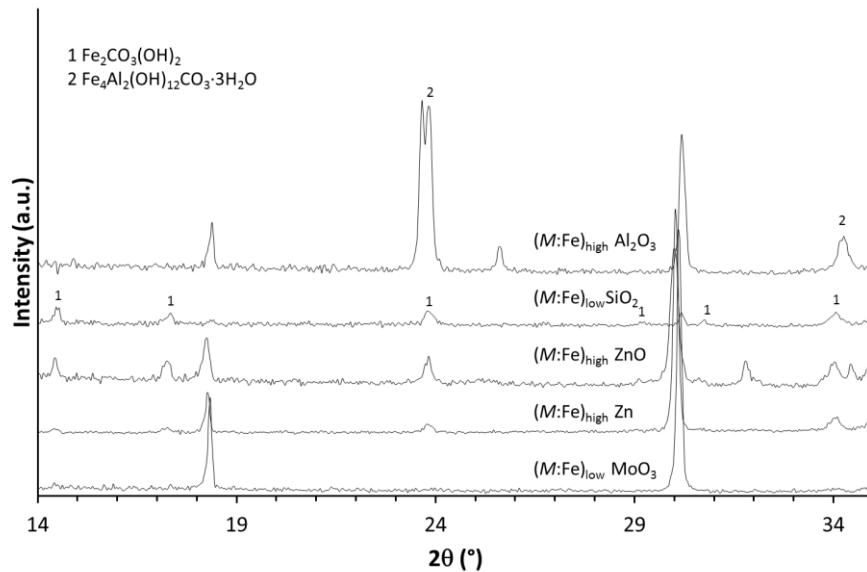
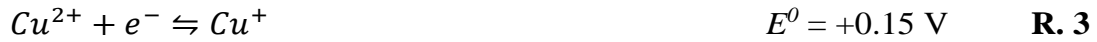


Figure 10. XRD diffractograms of the solid residues after hydrothermal treatment containing carbonate hydroxide phases.

### 3.2.2.3 Inhibition through redox effects

In the presence of  $\text{CuO}$  ( $(M:\text{Fe})_{\text{high}}$ ), hydrogen production only initiated after 8.9 h (Figure 4). Furthermore, a significant lower hydrogen gas yield (57%) and a

significant higher  $k$  (3.3 bar h<sup>-1</sup>) were obtained in comparison to the reference experiment (76% and 2.8 bar h<sup>-1</sup>, respectively) (Figure 5, Supplementary Data). XRD analyses showed that the CuO was reduced to metallic Cu (Figure 11), which was confirmed by SEM-EDS analyses (Supplementary Data). Cu is more noble than Fe, hence Fe reduces CuO *via* electron transfer. Besides, an experiment was performed for a shorter reaction time of 2 h in order to study intermediate reaction products in the solid phase. In the obtained solid, Fe, Fe<sub>2</sub>O<sub>3</sub>, CuO, Cu<sub>2</sub>O and Cu were detected as crystalline phases *via* XRD analyses (Figure 11). Hence, the reduction of CuO to Cu –with Cu<sub>2</sub>O as intermediate– seems to take place together with the oxidation of Fe to iron(III) oxide/hematite Fe<sub>2</sub>O<sub>3</sub>. Therefore, the following half reactions (R. 3 – 6) are proposed to be relevant.



However, after a 16 h experiment with ( $M:\text{Fe}$ )<sub>high</sub> CuO, no Fe<sub>2</sub>O<sub>3</sub> was found in the obtained solid *via* XRD analyses. Hence, Fe<sub>2</sub>O<sub>3</sub> is reduced back to Fe<sub>3</sub>O<sub>4</sub> *via*, for example, R. 7 and/or R. 8, once all CuO has reacted to form Cu.



Thus, the occurrence of a CuO-Fe redox system hinders the formation of hydrogen gas until all CuO is reduced to metallic Cu. The remaining metallic Fe then reacts with water to produce hydrogen gas and Fe<sub>3</sub>O<sub>4</sub>.

It needs to be noted that in the case of ( $M:\text{Fe}$ )<sub>high</sub> metallic Cu, the H<sub>2</sub> production yield was also reduced to 68% (Figure 5). The reduction in H<sub>2</sub> yield for this experiment can be ascribed to the presence of oxidised Cu (Cu<sub>2</sub>O) as an impurity in the metallic Cu powder (Supplementary Data), causing oxidation of metallic iron as described above.

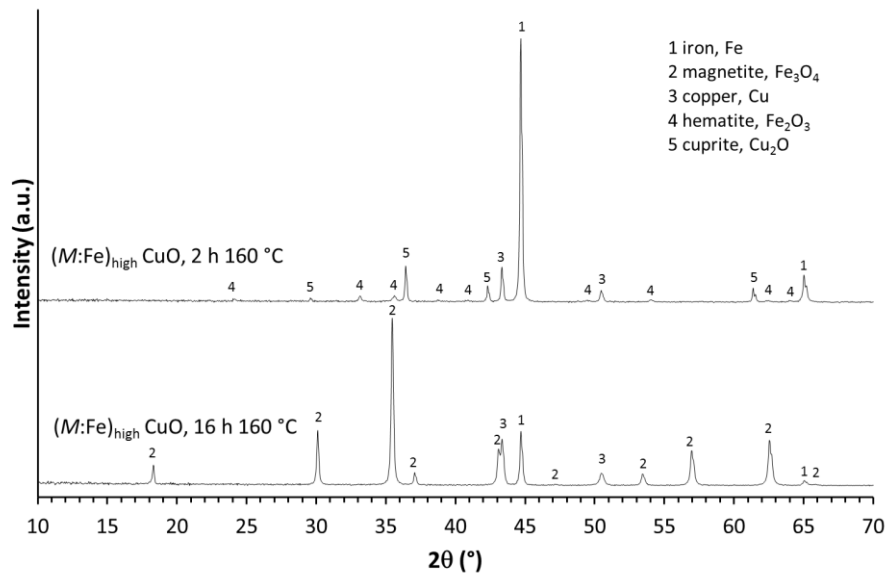


Figure 11. XRD of 2 h and 16 h reaction of (M:Fe)<sub>high</sub> CuO

In the presence of both V<sub>2</sub>O<sub>5</sub> and Co<sub>3</sub>O<sub>4</sub>, no hydrogen gas was formed during reaction, regardless of the added amounts, i.e. (M:Fe)<sub>low</sub> and (M:Fe)<sub>high</sub> (Figure 5). ICP-AES analyses on the reaction solution after reaction showed the presence of dissolved V (340 ppm) and Co (2 ppm). Both V<sup>5+</sup> and Co<sup>3+</sup> are strong oxidising agents in solution (R. 9-10).



Furthermore, V<sup>5+</sup> in solution hydrates and tends to deprotonate water as a function of pH, leading to acidification of the reaction solution [23]. It is expected that both species inhibit the oxidation reaction between water and metallic iron.

When V<sub>2</sub>O<sub>5</sub> was added to the reaction mixture, amorphous precipitates which contain K, V and O (Figure 12) were formed and EDS analyses suggest that K and V are present in a 3:7 molar ratio. Therefore, we assume that hydrothermal synthesis of a potassium vanadate material took place. Actually, hydrothermal synthesis of potassium vanadates has been reported in the literature to take place above 180 °C and 48 h [24, 25]. In the systems studied in this work, the applied reaction temperature and time were not sufficiently high and long, respectively, to allow for crystallisation of the potassium vanadate material.

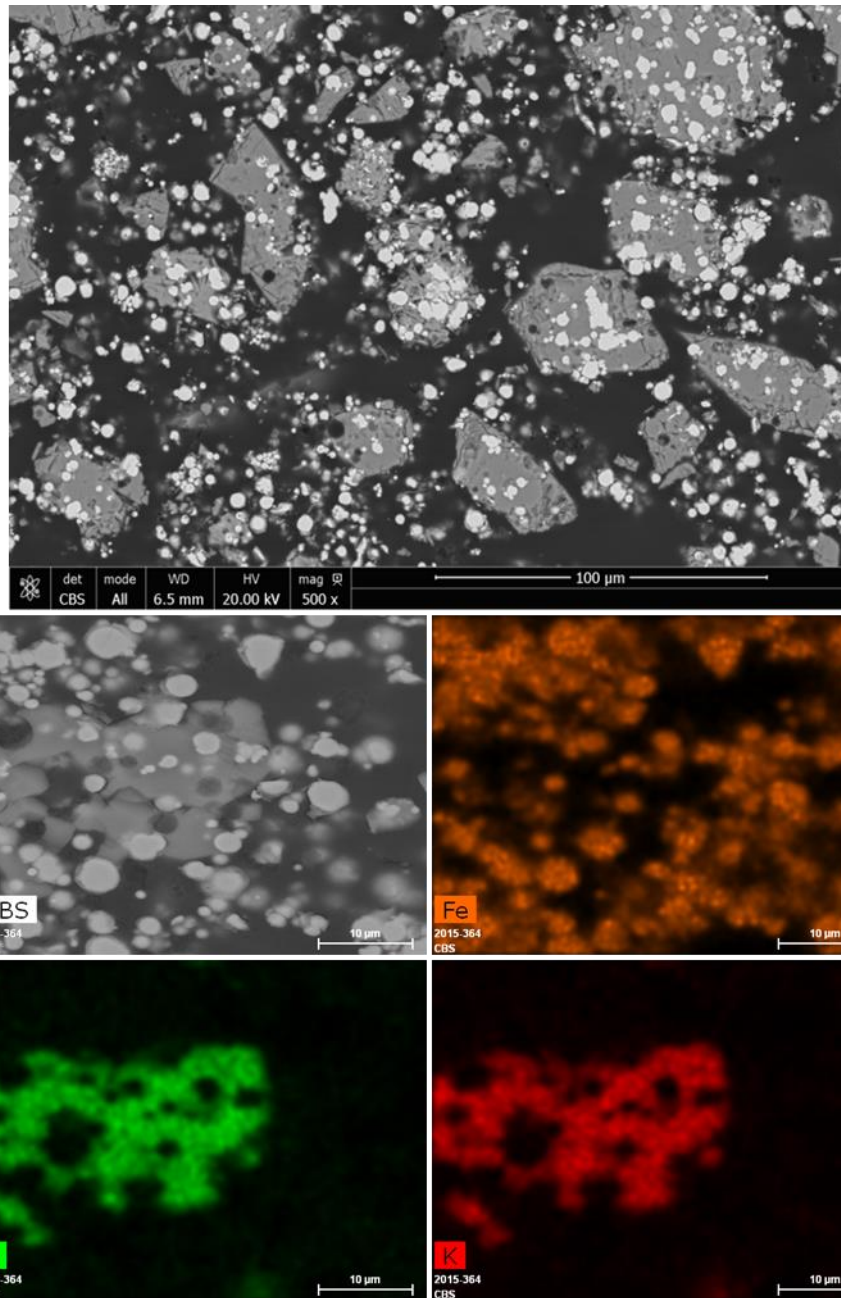


Figure 12. SEM-BSE and SEM-EDS images of the solid obtained through the  $(M:Fe)_{high}$   $V_2O_5$  experiment.

Upon  $Co_3O_4$  addition at a low concentration (i.e.  $(M:Fe)_{low}$ ) metallic iron oxidised to form  $Fe_3O_4$  (Supplementary Data), but no  $H_2$  gas was produced. Furthermore, SEM images of the obtained residue shows the presence of Co in its metallic zero-valent state (Figure 13), indicating that  $Co_3O_4$  is reduced by Fe through a cementation reaction [26]. The cementation reaction did not occur upon addition of  $Co_3O_4$  at high

concentration (i.e.  $(M:Fe)_{high}$ ) and only metallic Fe and  $Co_3O_4$  were present in the residue (Figure 13).

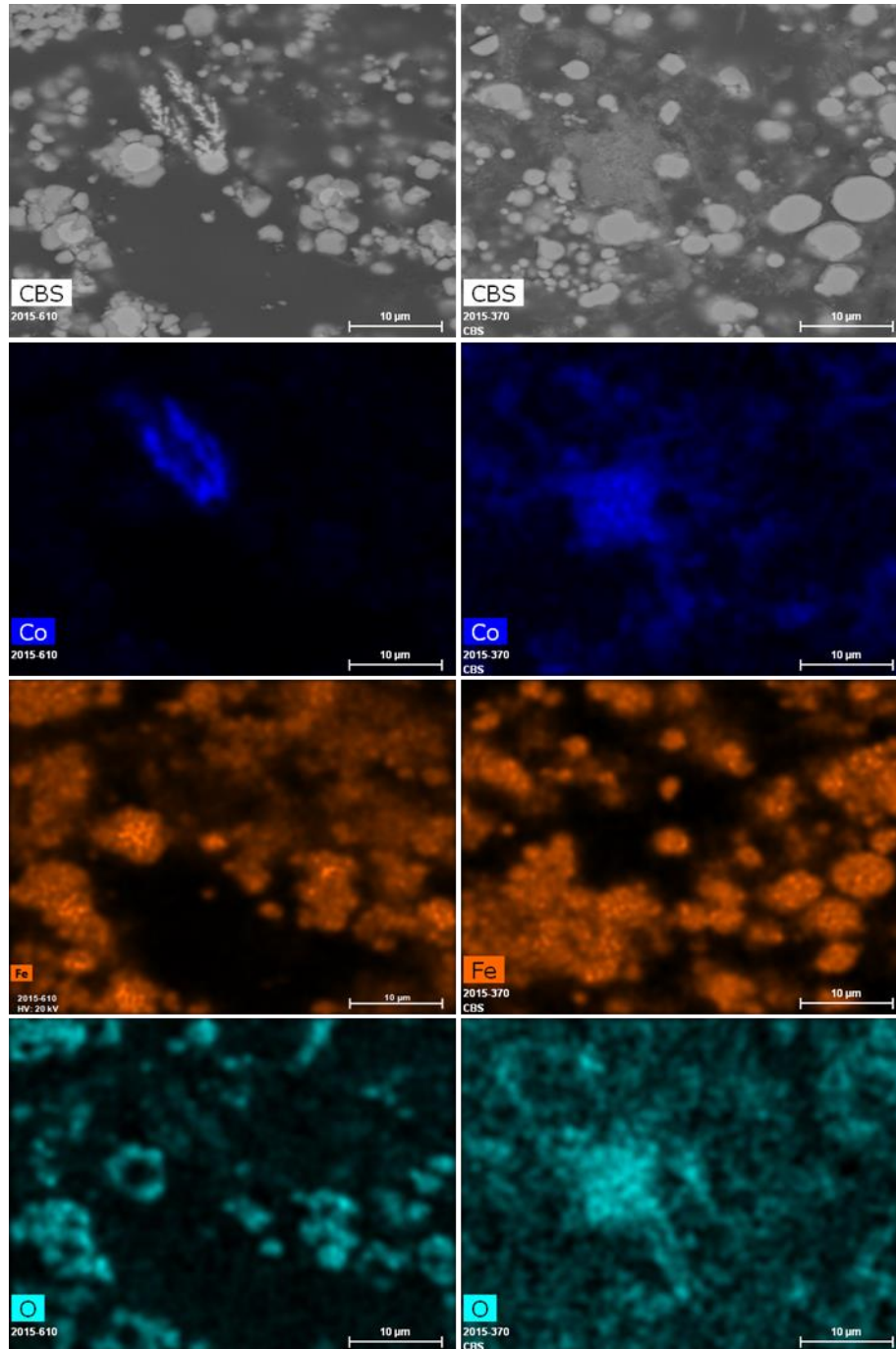


Figure 13. SEM-BSE and SEM-EDS images of the solids obtained through the  $(M:Fe)_{low}$   $Co_3O_4$  (left) and  $(M:Fe)_{high}$   $Co_3O_4$  (right) experiments.

### 3.3 Study of fine industrial metallic iron-rich waste powders

Figure 14 shows the pressure evolution curves for the hydrothermal reaction, wherein the metallic iron rich waste powders IWP-A, IWP-B and IWP-C were used as metallic iron source. No hydrogen production occurred in the presence of IWP-A, while IWP-B and IWP-C gave a modest  $H_2$  yield. Based on the composition and mineralogy of IWP-A (Table 1, Figure 1) and the gained knowledge on the influence of individual contaminants, we derive that the presence of  $SiO_2$  and possibly also  $Al_2O_3$  caused the inhibition of  $H_2$  gas formation. Whereas, IWP-B and IWP-C contained much lower quantities of Si (<1 wt%) a hydrogen gas production of 8 mmol and 11 mmol, respectively, was observed. When these produced amounts are compared to the  $H_2$  production potential of the two waste materials, respective  $H_2$  yields of 18% and 39% were reached (Table 4).

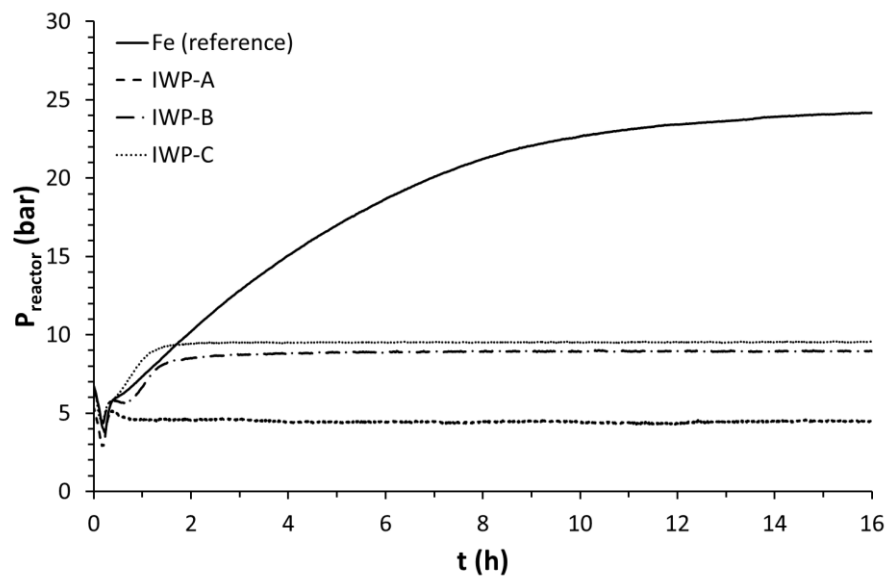


Figure 14. Evolutions in reactor pressure over time for the experiments applying fine industrial metallic iron-rich waste powder IWP-A, IWP-B and IWP-C.

Table 4. Obtained results related to the hydrogen gas production in the case of performing experiments with fine industrial metallic iron-rich waste powder IWP-A, IWP-B and IWP-C.

Parameter	Zero order fit				Boltzmann fit				Experimental parameters	
	$P_0$	$k$	range	$R^2$	$P'_0$	$P'_{max}$	$k'$	$R^2$	H <sub>2</sub> Yield (%)	$t_e$ (h)
IWP-A	n.d.	n.d.	n.d.	n.d.	n.d.	n.d.	n.d.	n.d.	0	n.d.
IWP-B	2.63	4.07	0.8;1.3	0.9979	2.59	8.91	2.43	0.97062	18	2.5
IWP-C	3.91	4.54	0.6;1.0	0.9986	5.06	9.52	3.84	0.99224	39	2.0

Both IWP-B and IWP-C have fast reaction rate constants ( $k$  and  $k'$ ) with respect to that of the reference experiment with pure metallic iron powder. Moreover, the production of hydrogen gas took place during the first 2-2.5 h (values of the effective reaction time  $t_e$ ). The reaction with IWP-B showed a time delay of approximately 15 min for the increase in pressure after the reaction temperature of 160 °C was reached. SEM and SEM-EDS images (Figures 15 and 16) show that iron particles in both powders clearly reacted and formed smaller iron oxide particles. However, most of the larger metallic iron particles (about >50  $\mu\text{m}$ ) reacted only at their surface, forming an iron oxide passivation layer at the grain boundaries (Figures 15 and 16). This finding is in line with previous studies showing that iron particles are ideally of small dimensions to allow for full oxidation in a hydrothermal reaction system [1, 2]. The metallic iron in the waste powders oxidised to  $\text{Fe}_3\text{O}_4$ , while wüstite ( $\text{FeO}$ ) did not react (Figure 17).

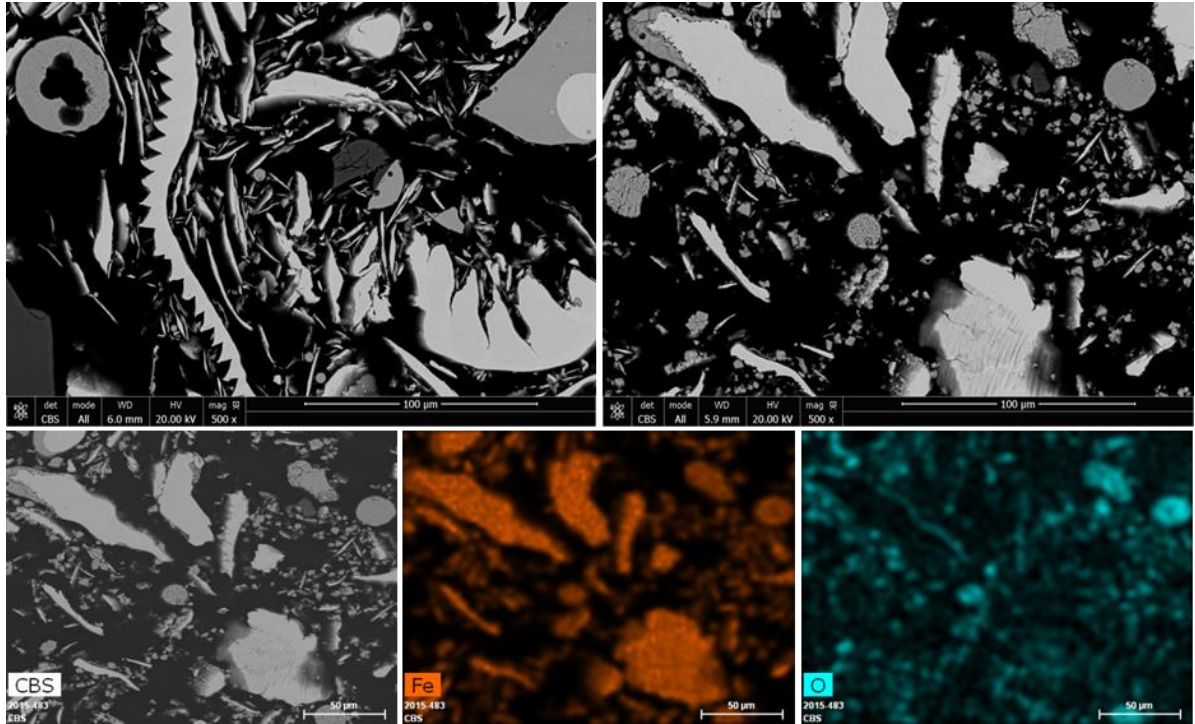


Figure 15. Top: SEM images of unreacted (left) and reacted (right) IWP-B. Bottom: SEM-CBS image (left) and SEM-EDS elemental mapping for Fe (middle) and O (right) of reacted IWP-B.

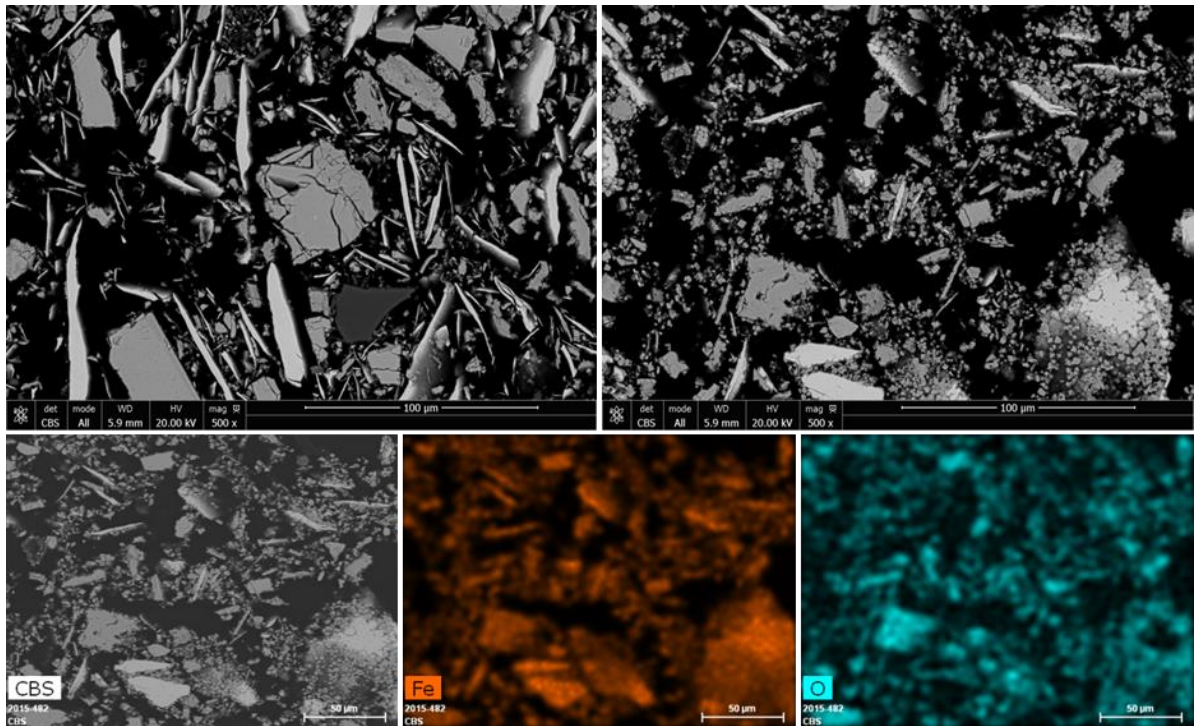


Figure 16. Top: SEM images of unreacted (left) and reacted (right) IWP-C. Bottom: SEM-CBS image (left) and SEM-EDS elemental mapping for Fe (middle) and O (right) of reacted IWP-C.

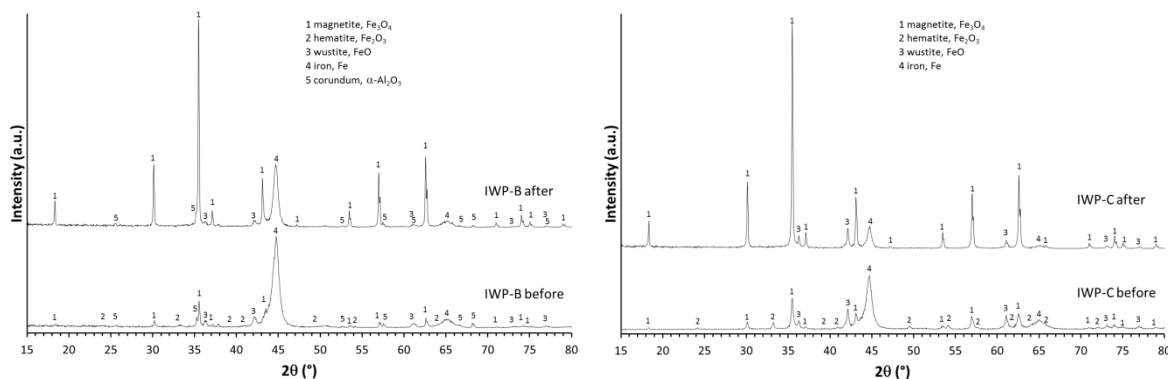


Figure 17. X-ray diffractograms of the IWP-B (left) and IWP-C (right) before and after hydrothermal reaction.

## 4 Conclusions

The oxidation of metallic iron particles and the consequent  $H_2$  gas production in the investigated hydrothermal reaction system can be inhibited through three main effects by the here studied contaminants, namely passivation of the reaction surface, carbonate precipitation and/or redox effects (Figure 18). Passivation occurs through the precipitation of a stable mineral layer at the surface of the iron particles, inhibiting water to react with the metallic iron surface. In this work, passivation layers consisted of (i) silicates, when  $SiO_2$  was present, (ii) iron spinels ( $MFe_2O_4$ ,  $M = Mo, Mn, Zn$  or  $FeAl_2O_4$ ), or (iii)  $Fe_3O_4$ . Carbonate precipitation removes carbonates, which have a catalytic role in the iron oxidation reaction under the here applied conditions, from the reaction solution and thus is expected to slow down the hydrogen production reaction kinetics. Several transition metal ions have competitive redox behaviours with the oxidation of iron by water. In particular, metallic iron cementates  $CuO$  and  $Co_3O_4$  to, respectively, metallic  $Cu$  and  $Co$ . Whereas  $V_2O_5$  exhibit both redox effects and formation of a potassium vanadate that passivates the iron particles.

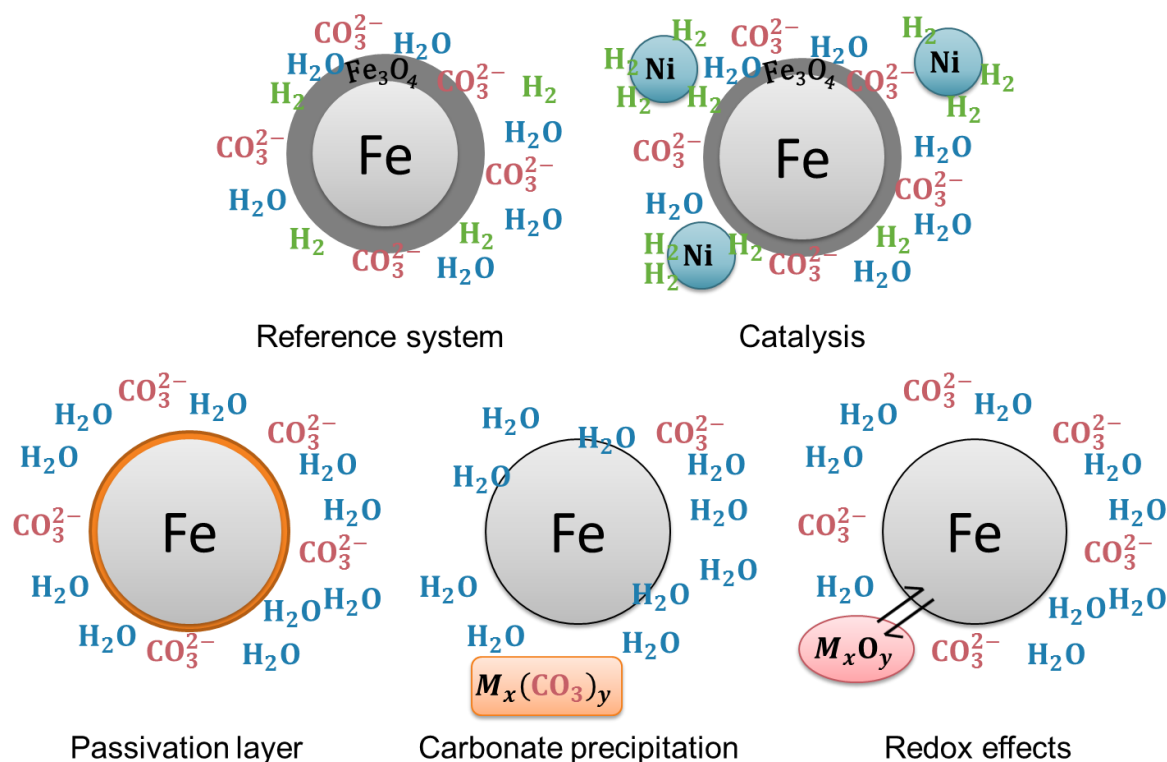


Figure 18. Representation of the model system, the Ni catalysed system and the three hydrothermal iron-oxidation inhibiting effects, observed in this work

Nickel has clearly shown to act as a catalyst. Addition of metallic Ni to the reaction mixture increased the reaction kinetics significantly and thereby shortened the reaction time from 16 h to below 6 h for a Ni addition of Fe:Ni = 0.01. However, Ni also increases the kinetics of Fe<sub>3</sub>O<sub>4</sub> precipitation at the surface of the metallic iron particles. Therefore, an excessive addition of Ni decreases the H<sub>2</sub> production yield due to fast passivation of the metallic iron reaction surface.

Finally, the application of 3 industrial iron waste powders (IWP-A, IWP-B and IWP-C) in the studied hydrothermal reaction system showed that the presence of 10 wt% SiO<sub>2</sub> in IWP-A completely inhibited H<sub>2</sub> production. Whereas, iron-rich IWP-B and IWP-C did yield 18% and 39% H<sub>2</sub> gas, respectively. These yields are moderate and the oxidation of metallic iron particles was incomplete due to the large grain sizes of the samples in addition to possible inhibiting effects. In conclusion, this work confirmed that metallic iron waste powders have preferentially small grain sizes for an optimal mild hydrothermal hydrogen gas production process. Furthermore, the presence of only limited amounts of contaminants in the waste powder is desired. Especially, SiO<sub>2</sub> and V, Mo or Co metals or oxides, show strong inhibiting effects. Of

course, the impact of each contaminant is determined by its content (wt%), type and way of occurrence.

## 5 Acknowledgements

The authors would like to gratefully acknowledge the trust and financial support of the Agency for Innovation by Science and Technology in Flanders IWT (Ph.D. grant No. 111324). In addition, the authors greatly appreciate the expertise and constructive discussions provided by Raymond Kemps and Myrjam Mertens of VITO, who have performed SEM measurements and XRD analyses, respectively.

## 6 References

1. Michiels, K., J. Spooren, and V. Meynen, *Production of hydrogen gas from water by the oxidation of metallic iron under mild hydrothermal conditions, assisted by in situ formed carbonate ions*. *Fuel*, 2015. **160**: p. 205-216.
2. Liu, L.-H., Y.-C. Tsai, and D.-H. Chen, *Catalyst-enhanced hydrothermal generation of highly pure compressed hydrogen gas from iron micro-powders*. *RSC Adv.*, 2016. **6**(90): p. 86938-86942.
3. *Höganäs Handbook for Sintered Components*, in *PM-SCHOOL HANDBOOK 1*, H. AB, Editor. 2013, Höganäs AB.
4. *WasteResource*. [cited 13th of June 2016; Available from: <http://www.residuorecurso.com/en/anunci/veure/2682>].
5. Das, S., et al., *Synthesis and properties of a novel structural binder utilizing the chemistry of iron carbonation*. *ACS Appl Mater Interfaces*, 2014. **6**(11): p. 8295-304.
6. Crouzet, C., et al., *Hydrothermal Valorization of Steel Slags—Part I: Coupled H<sub>2</sub> Production and CO<sub>2</sub> Mineral Sequestration*. *Frontiers in Energy Research*, 2017. **5**.
7. Zenkov, V.S., V.V. Pasichnyi, and V.P. Red'ko, *Reduction of iron-containing metallurgical waste to obtain hydrogen with iron vapor method*. *Powder Metallurgy and Metal Ceramics*, 2009. **47**(11-12): p. 733-742.
8. *The International Center for Diffraction Data*. 6th of January 2015]; Available from: <http://www.icdd.com>.
9. *The Inorganic Crystal Structure Database*. 6th of January 2015]; Available from: <https://icsd.fiz-karlsruhe.de>.
10. *The Stainless Steel Information Center*. 12th of November 2016]; Available from: [http://www.ssina.com/overview/alloyelements\\_intro.html](http://www.ssina.com/overview/alloyelements_intro.html).
11. Rabenau, A., *THE ROLE OF HYDROTHERMAL SYNTHESIS IN PREPARATIVE CHEMISTRY*. *Angewandte Chemie-International Edition*, 1985. **24**(12): p. 1026-1040.
12. Levenspiel, O., *Fluid-Particle Reactions: Kinetics*, in *Chemical reaction engineering*, W. Anderson, Editor. 1999, John Wiley & Sons: New York. p. 566-588.
13. Tsai, Y.-C., L.-H. Liu, and D.-H. Chen, *Hydrothermal generation of compressed hydrogen gas by iron powders*. *RSC Adv.*, 2016. **6**(11): p. 8930-8934.
14. Gong, M., et al., *A mini review on nickel-based electrocatalysts for alkaline hydrogen evolution reaction*. *Nano Research*, 2015. **9**(1): p. 28-46.
15. Chen, K.-F., S. Li, and W.-x. Zhang, *Renewable hydrogen generation by bimetallic zero valent iron nanoparticles*. *Chemical Engineering Journal*, 2011. **170**(2-3): p. 562-567.
16. Faivre, D., *Iron Oxides: From Nature to Applications*. 2015: Wiley - VCH. 632.

17. Brik, M.G., A. Suchocki, and A. Kaminska, *Lattice parameters and stability of the spinel compounds in relation to the ionic radii and electronegativities of constituting chemical elements*. Inorg Chem, 2014. **53**(10): p. 5088-99.
18. [20th of June 2016]; Available from: <http://www.mindat.org/>.
19. Yi, X., et al., *Hydrothermal preparation and characterization of ultrafine powders of ferrite spinels  $MFe_2O_4$  ( $M = Fe, Zn$  and  $Ni$ )*. Materials Science and Engineering: B, 1995. **34**(1): p. L1-L3.
20. Kongmanklang, C. and K. Rangsriwatananon, *Facile Hydrothermal Synthesis of Size-Controlled Silicalite Crystals from Rice Husk Ash*. Journal of Chemical Engineering of Japan, 2016. **49**(8): p. 799-804.
21. Azoulay, I., C. Rémazeilles, and P. Refait, *Determination of standard Gibbs free energy of formation of chukanovite and Pourbaix diagrams of iron in carbonated media*. Corrosion Science, 2012. **58**: p. 229-236.
22. Chen, R., et al., *Formation of chukanovite in simulated groundwater containing  $CO_3^{2-}$* . Environ Technol, 2016: p. 1-7.
23. Livage, J., *Hydrothermal Synthesis of Nanostructured Vanadium Oxides*. Materials, 2010. **3**(8): p. 4175-4195.
24. Feng, B., et al., *A Simple Method for the Synthesis of  $KV_3O_8 \cdot 0.42H_2O$  Nanorod and Its Lithium Insertion/Deinsertion Properties*. International Journal of ELECTROCHEMICAL SCIENCE, 2013. **8**: p. 1095 - 1102.
25. Oka, Y., Y. Takeshi, and N. Yamamoto, *HYDROTHERMAL SYNTHESIS AND STRUCTURE REFINEMENTS OF ALKALI-METAL TRIVANADATES  $AV_3O_8$  ( $A = K, Rb, Cs$ )*. Materials Research Bulletin, 1997. **32**(9): p. 1201-1209.
26. Addy, S. and A.J. Fletcher, *The Deposition of Cobalt on Iron-Powder by Means of the Cementation Reaction*. Hydrometallurgy, 1987. **17**(3): p. 269-280.